RESEARCH ARTICLE

The multi-scale influence of topography on lava flow morphology

Paul Richardson[1,2] · Leif Karlstrom[1]

Abstract

Predicting lava flow pathways is important for understanding effusive eruptions and for volcanic hazard assessment. One particular challenge is understanding the interplay between flow pathways and substrate topography that is often rough on a variety of scales (< 1 m to 10 s km). To study this problem, we develop a lava flow modeling framework that combines spectral analysis of substrate roughness with a new lava flow model (MULTIFLOW). The MUTLIFLOW model includes a multiple flow direction routing algorithm in conjunction with a thresholding function that limits the extent of the flow. Comparison of MULTIFLOW results with recent flows on Mt. Etna, Mauna Loa, and K̄īlauea suggests that MULTIFLOW accurately predicts the influence of topography on lava flow paths and morphology. Spectral filtering of pre-flow digital elevation models allow us to quantify which topographic wavelengths are most important for influencing lava flow pathways. Filtering constrains the height of pre-existing objects that flow overtop as a measure of flow thickness, and aids in identifying divergence of flow pathways from pre-eruptive topography that would result from modification of the substrate by the flow. Low-pass filter cutoffs in the range of ∼ 10–100 m significantly improve the fit between modeled flow and real flow paths, suggesting a sensitivity of lava flow paths to such mesoscale topographic wavelengths. The three case studies are generalized with a parameter investigation of lava flow branching on synthetic red-noise topography. We demonstrate that the tendency of a flow to branch or not can be predicted on the basis of spectral characteristics of the underlying surface. We end by examining spectral signatures associated with volcanic and erosional processes on the Island of Hawai'i that may aid in forecasting lava flow pathways and deconvolving competing topographic construction and erosion in volcanic landscapes on longer timescales.

Keywords Lava flows · Volcanic hazards · Volcanic landscape evolution · Change detection · Flow routing · Topographic roughness

Introduction

Lava flows are shaped both by intrinsic fluid dynamics and by the extrinsic characteristics of the topographic substrate over which flow occurs (e.g., Walker 1973; Soule et al. 2004; Cashman et al. 2013). The degree to which one versus the other controls lava flow morphology on all scales, from flow pathways to overall planform shape, is not well understood. At small (< ∼ 1 m) scales, subaerial lava flows are often

categorized by their surface texture, for example as p̄āhoehoe or `a`ā flows for basaltic lava (e.g., Peterson and Tilling 1980; Kilburn 1981; Lipman and Banks 1987; Hon et al. 1994). Morphology is determined by emplacement conditions such as effusion rate and surface slope (e.g., Griffiths 2000; Katz and Cashman 2003; Soldati et al. 2016), as well as cooling rate, magma melt composition, and presence of crystals (e.g., Cashman et al. 1999; Riker et al. 2009; Chevrel et al. 2018).

At the largest scales, where field mapping and remote sensing constrain the distribution of large-scale lava flow planform shapes (e.g., Wolfe et al. 1988; Coltelli et al. 2007; Karlstrom et al. 2018), flow area and mass flux from the volcanic vent tend to be correlated (e.g., Walker 1973; Pieri and Baloga 1986; Soule et al. 2004). At scales smaller than planform area, there is much diversity in lava flow shapes. Lava flow length is controlled by intrinsic properties of the eruption, magma rheology, and underlying slope (e.g., Pinkerton and Wilson 1994; Slezin 2008; Harris and Rowland 2009; Deardorff and Cashman 2012). Lava flow width is less well understood, but may be

---

✉ Leif Karlstrom
  leif@uoregon.edu

1   Department of Earth Sciences, University of Oregon, Eugene, OR, USA

2   US Forest Service Pacific Southwest Research Station, Redwood Sciences Laboratory, Arcata, CA, USA

largely controlled by characteristics of the underlying surface (e.g., Hulme 1974; Guest et al. 1987; Kerr et al. 2006). Lateral dispersivity also affects the local slopes thought to influence transitions in flow style between `a`ā and pāhoehoe of later flows or flow lobes (e.g., Kilburn 1981; Soule et al. 2004; Cashman et al. 2013). Width is further complicated by branching and braiding structures in lava flows and the time-variable nature of flow lobe emplacement and solidification (Dietterich and Cashman, 2014).

Existing lava flow models are of two types: there are those that solve a 2D or 3D flow/thermal problem ("physics-based models") and those that use parameterizations of the physics to leverage flow routing on digital elevation models ("rules-based models"). Physics-based models (e.g., Harris and Rowland 2001; Del Negro et al. 2008; Harris et al. 2011; Bilotta et al. 2016; Dietterich et al. 2017; Chevrel et al. 2018) should eventually produce the most accurate flow paths and predict thickness variations. However, processes governing transition between flow styles, crust, or lava tube development, and role of flux variations on flow thickness require further study. Although there are exceptions, these models often have the disadvantage of being computationally expensive (see Cordonnier et al. 2016 for discussion).

Rules-based models (e.g., Favalli et al. 2005; Vicari et al. 2007; Mossoux et al. 2016) may be probabilistic or deterministic, have significantly improved computational efficiency, and still capture many features of lava flow propagation through parameterizations of physics (a "hybrid" modeling approach). But such models often do not intrinsically account for the finite length of flows or flow thickness, and often must be calibrated empirically for each application. Rules-based models capable of predicting lava flow pathways and extent are currently used to forecast lava flows by some volcano observatories (Vicari et al. 2007; Patrick et al. 2016) due to their efficiency and the ease by which predictions may be updated in near real time (Poland et al. 2016). Such models are an appealing choice for applications that require many thousands of computations for large digital elevation models (DEMs) over extended areas and long-term volcanic landscape evolution simulation, or for forecasting lava flows during an on-going eruption when the topography actively changes through time.

For both classes of models, including the hybrid approach that parameterizes physics in rules-based models, a primary challenge thus lies in synthesizing flow over rough topography with realistic flow mechanics. Pre-existing topography includes preexisting vent constructs and prior lava flows, prior surface features such as lava channels, tumuli, or pressure ridges (Applegarth et al. 2010; Rumpf et al. 2018), vegetation (Deligne et al. 2013), and erosional features such as fluvial channels (Ferrier et al. 2013a, b). These structures are highly variable among volcanoes.

Here, we seek to understand how topography influences lava flow topology, by quantifying the scale dependence of surface roughness and signatures of flow interaction with rough topography. We apply spectral techniques to quantify two characteristics of lava flow-dominated landscapes: topographic variance and spectral slope. We compute these metrics for recent lava flows on Mt. Etna volcano, Italy, and Mauna Loa and Kīlauea volcanoes (USA) demonstrating that these cases are well characterized by a red-noise topographic amplitude spectrum. Identification of spectral metrics then guide a numerical investigation of how topography influences lava flow pathways at a range of spatial scales.

In doing this, we present a new lava flow emplacement model (MULTIFLOW) that combines the multiple flow direction (MFD) flow algorithm (Freeman 1991) to disperse lava across a DEM with a thresholding function which limits the extent of the flow. MULTIFLOW is tested and calibrated for three test cases where pre- and post-flow DEMs exist, including a lava flow on Mt. Etna that has become a community benchmark for testing lava flow models (Cordonnier et al. 2016). We generalize these applications by creating a series of synthetic landscapes with topographic spectra that mirror real flows, as a testbed to systematically explore the degree of branching produced by MULTIFLOW model runs over variable topography. We find that the degree of flow branching is predictable based on the variance and spectral slope parameters of these synthetic landscapes. This suggests that lava flow prediction may be improved by understanding the controls on topographic roughness. We conclude by investigating spectral signatures of constructional and erosional features for volcanic landscapes on the Big Island of Hawai'i. Both constructional and erosional features are distinguishable in the spectral domain, with a systematic dependence of roughness on flow age.

Methods

Digital elevation models of pre-flow and post-flow topography

We analyze three lava flows where DEMs were collected prior to lava flow emplacement and again after the lava flow occurred (Fig. 1). Slopes reported in this section are calculated as the slope of the best-fit plane fit to the regions outlined in Fig. 1. We note that slope depends on the length scale over which it is measured for natural surfaces. In all cases, post-flow topography is more accurate than the pre-flow topography.

The Mt. Etna DEM covers the "Lower Fissure System 1" flow of the 2001 Etna eruption, the first major flow of the Lower Fissure System which included the most active effusive venting of the 2001 eruption. Flows originated from four different vent locations along a complex fracture system and we

Fig. 1 Shaded relief map of **a** Mt. Etna with the 2001 lava flow outlined in black, **b** the flank of Mauna Loa with the 1984 lava flow outlined in black, and **c** the flank of K̄īlauea, HI with the 2011 lava flow of interest outlined in black. For K̄īlauea, we created the shaded relief from DEM data smoothed with a 100 m low-pass filter. The dashed box shows the region for which the background slope, spectral slope (β), and variance was calculated for data in panels **d**–**f**. Spectral results for **d** Mt. Etna, **e** Mauna Loa, and **f** K̄īlauea. Data are shown in gray. Due to the large number of data points, we randomly select a subset and show 10% for Mt. Etna and K̄īlauea and 1% for Mauna Loa. The slope of the line is fit to the binned data using an iteratively reweighted least squares regression
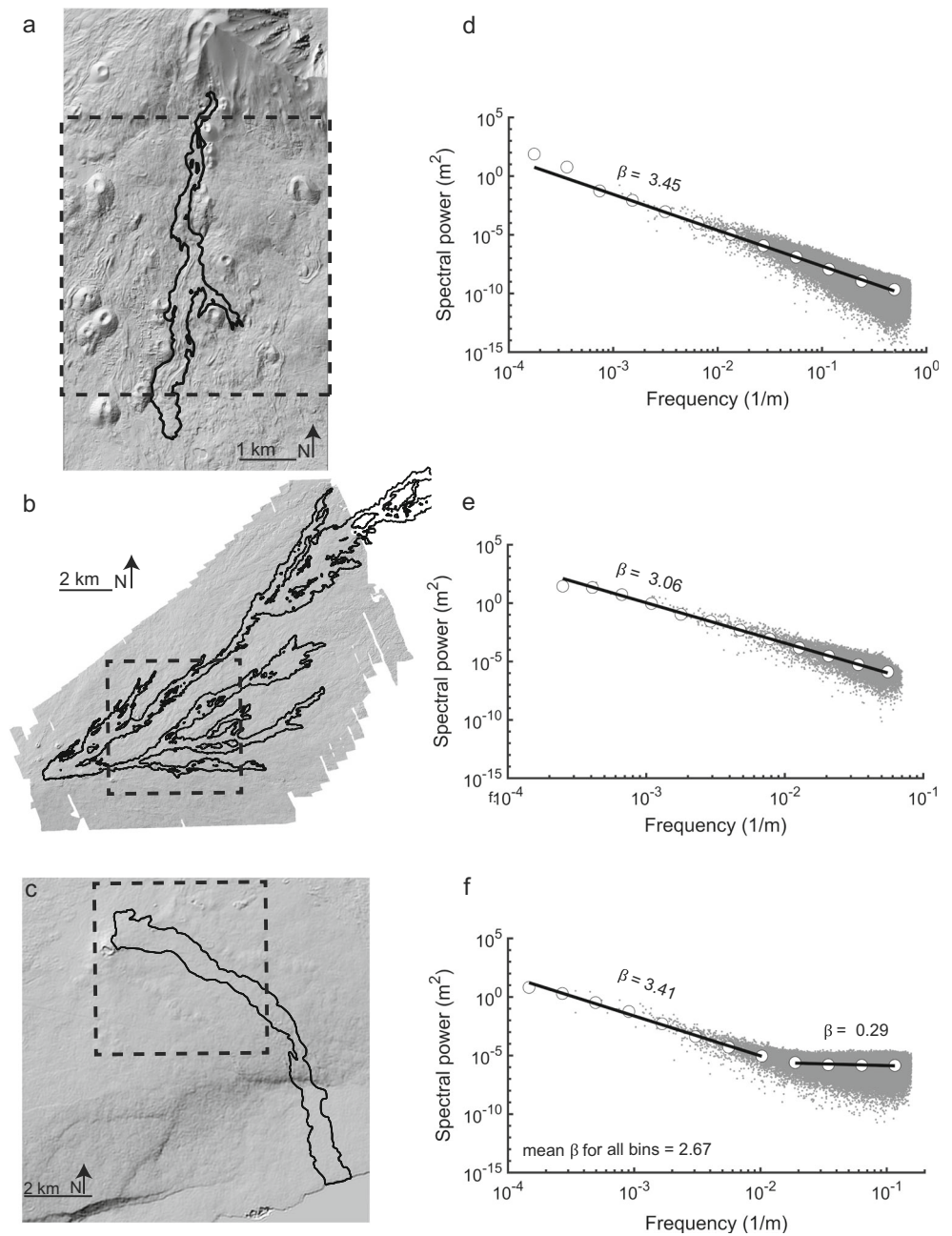
focus on the flow that originated from a vent at an elevation of 2100 m (Favalli et al. 2005). This flow was emplaced continuously between July 18 and August 9, 2001, with an average effusion rate of ~ 11.5 m³/s, average thickness of 11 m, and maximum length of 6.4 km (Fig. 1a) (Coltelli et al. 2007). The 2001 Etna eruption involved several compound flow fields including the Lower Fissure System 1 flow, which was dominated by a large axial lava channel and several spillovers (Favalli et al. 2005). The background slope near this flow is 9.7° (Fig. 1). The pre- and post-flow DEMs from this flow have been proposed as a community benchmark for lava flow models (Cordonnier et al. 2014), and has been used as such by several authors (e.g., Favalli et al. 2005; Cordonnier et al. 2016; de'

Michiele Vitturi and Tarquini 2018). The pre-flow DEM data was collected in 1999, while the post-flow data was collected in 2001. Both 10 m resolution DEMs were constructed from vector contour maps produced photogrammetrically from aerial surveys (Coltelli et al. 2007). The outline of the lava flow was supplied by the Istituto Nazionale di Geofisica e Vulcanologia (Tarquini and Favalli 2011).

The 1984 Mauna Loa flow on the Big Island of Hawai'i occurred between March 25 and April 14, 1984, with four different branches active throughout that period (Lipman and Banks 1987). The mean effusion rate was ~ 275 m³/s and the final flow length was ~ 27 km (Fig. 1b) (Lipman and Banks 1987; Crisp et al. 1994). Flow thickness was on average 1–

4 m, with local thickness in excess of 20 m (Dietterich and Cashman 2014). The emplacement of each branch was time-progressive, although the distributary nature of the flow did not result in significant overlapping flow pathways between branches. The slope near these flows is 5.1°.

We use a DEM with 10 m resolution of the 1984 Mauna Loa flow created from pre-eruptive stereo images (USGS-sourced areal photographs from 1977, Dietterich and Cashman 2014). High-resolution LiDAR (Light Detection And Ranging) data collected by the National Center for Airborne Laser Mapping in 2009 is used as the post-flow DEM. We resample the LiDAR to a grid resolution of 10 m to match the pre-eruptive grid resolution and flow outlines.

The example lava flow from Kīlauea on the Big Island of Hawai'i used in our study originated from the Pu'u 'Ō'ō vent, as part of a persistent effusive eruption between 2011 and 2013. We focus on lava that erupted from a fissure, often referred to as the Peace Day vent (Poland 2014), that opened on the flank of the Pu'u 'Ō'ō cone on September 21, 2011 (Fig. 1c). This long-lived pahoehoe flow field reached the Pacific Ocean on December 9, 2011, with a final length of ~ 8 km. Flow field depth was 10–15 m (maximum of ~ 30 m) in the center of the flow, but thinned to ~ 1 m near flow margins (Poland 2014). This flow was the dominant active flow for ~ 15 months until the Kahauale'a flow became active in January 2013, with Peace Day flows waning during the last few months of 2013 (Kauahikaua and Hawaiian Volcano Observatory staff 2016). Slopes within this flow field are 2.3°.

The pre-2011 Kīlauea DEM is from airborne interferometric SAR ("IfSAR") data collected in 2005 by the National Oceanic and Atmospheric Administration, while the post-eruption data are TanDEM-X derived DEMs from the German Space Agency syn-eruptive bi-static SAR acquisitions during 2011–2013 (Poland 2014). We focus on lava deposition that occurred within the TanDEM-X acquisition period of September 15–December 23, 2011 (from which the flow outline was produced), which does not encompass the entire eruptive period (Poland 2014). The data is gridded to 4.5 m resolution, but noise appears more common in this DEM than others used here, with a broadening and flattening of the power spectrum at short wavelengths (Fig. 1).

The Mauna Loa flow exhibits a significantly more pronounced branching structure than the Kīlauea or Etna flows. However, the emplacement parameters of these flows were not the same. For example, the Mauna Loa flow was short-lived compared to the Kīlauea flow, which was active for months along the same path. The Mauna Loa flow generated four branches that were contemporaneous in time, unlike the Etna flow. Such differences in emplacement histories, along with characteristics of the substrate, compete to govern the planform morphology of the flows.

Spectral analysis applied to lava flow DEMs

Quantitative geomorphology is undergoing a revolution resulting from increased accuracy and prevalence of high spatial resolution topographic data (Roering et al. 2013). Among many other benefits of digital terrain models is the ability to apply more sophisticated signal processing tools to topography, which increases the quantification of landscape form and opens up new ways to compare with model predictions. We use the 2DSpecTools toolkit developed by Perron et al. (2008), which is based on a 2D discrete Fourier transform (DFT) (Press et al. 2007), to perform spectral analysis and filtering of DEMs and to create synthetic topography. The code is written in MATLAB and freely available (see code availability section).

As a preprocessing step, we detrend the topography by subtracting a best-fit plane (that used to compute background slopes), and pad the DEM with zeros so that the dimensions are in powers of two. For irregularly shaped DEMs such as Mauna Loa, we smoothly extrapolated the boundaries out from the edge of the data to the smallest rectangular grid that encompasses the entire DEM. The topography is also tapered by a Hann window (Press et al. 2007) to limit edge effects.

Detrending and tapering DEMs better satisfy the assumption of periodic boundaries inherent to the DFT. However, spectral ringing (Gibbs phenomenon) still often occurs near the boundaries. To further reduce edge effects, we apply the DFT to a larger region than we are interested in and remove a border (affected by the tapering window) after filtering. To generate this larger region, we mirror 2 km of topography along the rectangular DEM boundary, but limit our analysis to within the boundaries of the original DEM.

For some experiments, we low-pass filter the DEM. The filter exponentially tapers from one to zero between the frequencies F_L and F_H representing low (L) and high (H) filter bounds. We set $F_L = 1/(1/F_H + dx)$ where dx is the grid spacing of the DEM and use this definition of F_L unless otherwise noted.

Spectral metrics

We focus on two values to characterize the topography in the spatial frequency domain: (1) the spectral power, which describes the topographic amplitude of DEM features, and (2) the spatial frequency of the associated feature. These two values are related by the spectral slope (Fig. 1).

Many natural landscapes are characterized by a distribution of topography in which landforms with longer lateral dimension or wavelength have larger height (amplitude). We use a "red noise spectrum" model for such behavior, for which spectral power P is proportional to topographic amplitude at a given wavelength squared. Spectral

power varies inversely with spatial frequency f (inverse wavelength) as

$$P(f) \propto f^{-\beta} \qquad (1)$$

In landscapes for which Eq. 1 holds, the exponent β is related to the fractal dimension of the surface (Huang and Turcotte 1990), governing the rate at which landform height decreases with wavelength. Spectral slope $\beta = 0$ is the white noise spectrum, $\beta = 3$ landscapes are self-similar (aspect ratio of landforms is invariant), while other non-zero values of β indicate self-affine behavior. For example, $\beta > 3$ indicates that shorter wavelength features have larger width-height ratios than larger wavelength features. A fractal landscape will exhibit $2 \le \beta \le 4$ for all wavelengths of topography with no concentrations of power at particular wavelength bands (Perron et al. 2008). In real landscapes that deviate from fractal behavior, and many do (e.g., Wegmann et al. 2007; Perron et al. 2008; Crozier et al. 2018), concentrations of spectral power at particular wavelengths are often indicative of process. Erosional landscapes that are characterized by soil-mantled hillslopes and incised fluvial channels often exhibit comparable spectral slopes ($\beta \sim 3$) for frequencies below ~ 0.005 m^{-1} (~ 200 m wavelength) while higher frequencies exhibit a steeper spectral slope ($\beta = 4.5$–5) (Perron et al. 2008).

In addition to β, we are interested in the topographic variance (height of landscape roughness features). Total topographic variance is equal to the integral of the power spectrum over the frequency range for which the DEM has resolution. For experiments with lava flow routing over synthetic landscapes, we choose a β and also normalize topography by a specified variance to scale landscape roughness heights. We also calculate these metrics for real DEMs on Mauna Loa, Kīlauea, and Mt. Etna. For these cases, we bin the discrete spectra into 12 bins and report the slope of the binned data.

Topography and spectral characteristics of lava flows on the Big Island of Hawai'i and Mt. Etna

For Kīlauea, we complete spectral analysis of the pre-flow topography gridded to 4.5 m resolution. For Mauna Loa, we analyze the LiDAR-derived post-flow DEM gridded to 1 m resolution. For all case study sites, we assume that the spectral characteristics are likely similar before and after the lava flow emplacement event since both regions are covered with young lava flows (Sherrod et al. 2007). For Mt. Etna, we analyze the post-flow DEM gridded to 10 m resolution.

Topographic variance increases with the spatial area considered (consistent with the red-noise spectrum model), so we choose a characteristic horizontal scale for which to calculate variance of 5 km to compare the variance between study sites. For both Mauna Loa and Kīlauea, we characterize the topography for a detrended 5×5-km region that encompasses the flow

(Fig. 1 and Table 1). For Mt. Etna, our analysis is limited to a slightly smaller region of 4.75×5 km due to the limitations of available topography (Fig. 1). We choose to focus our analysis when possible on a 5×5-km region as the dimension approximates the maximum width of the 1984 Mauna Loa flow.

Although the region analyzed for Mt. Etna is slightly smaller than the regions for Mauna Loa and Kīlauea, the topographic variance is the highest (1220 m) while variance for Mauna Loa and Kīlauea are more comparable (752 m and 546, respectively).

We calculate spectral slope by performing a least squares fit to log-transformed and binned power spectra of each study site DEM (Fig. 1d–f). For the Kīlauea topography, the spectral slope for frequencies $< \sim 0.01$ m^{-1} (~ 100 m wavelength) is 3.41 and tails off to 0.29 at higher frequencies. The spectral slope for Mt. Etna is similar to the dominant trend of Kīlauea at 3.45, while the Mauna Loa flow field has a slightly lower spectral slope of 3.06. We do not see a significant falloff in spectral slope for the Mauna Loa or Mt. Etna DEMs.

Model development

MULTIFLOW lava flow routing algorithm

To explore lava flow pathways as a function of substrate characteristics, we develop a new lava flow model (MULTIFLOW) that uses the multiple flow direction (MFD) routing algorithm (e.g., Freeman 1991; Quinn et al. 1991; Tarboton 1997) in

Table 1 Summary of relevant lava flow and topographic characteristics

	Mt. Etna	Mauna Loa	Kīlauea
Topography[a]			
Variance (m^2)	1220	753	546
Spectral slope (β)	3.45	3.06	3.41[b]
Background slope[c] (°)	9.7	5.1	2.3
Lava flow[d]			
Mean flow thickness (m)	11[e]	4.4[g]	2.8
Flow length (km)	7[f]	27[g]	12[h]

[a] Values are measured within a 5×5-km region that encompass part of the flow for Mauna Loa and Kīlauea and within a 4.75×5 km region for Mt. Etna (see Fig. 1). Variance is measured for the detrended surface

[b] Spectral slope for frequencies $> \sim 0.01$ m^{-1}

[c] Background slope is calculated as the slope of the best-fit plane for the same region that we calculated the variance and spectral slope

[d] We report on the 1984 Mauna Loa flow, the cumulative flow deposits that occurred from September 15—December 23, 2011 for Kīlauea, and the 2001 Mount Etna flow of interest

[e] Coltelli et al. (2007)

[f] Behncke and Neri (2003). Mean flow thickness calculated by dividing reported volume by area

[g] Dietterich and Cashman (2014)

[h] Measured in Google Earth Pro

combination with a nonlinear threshold function that can be tuned to produce different flow morphologies and lengths (Fig. 2 and Table 2). From a given cell with linear index j on a rectangular grid, a flow routing algorithm will partition local flow among neighboring downslope cells (Quinn et al. 1991). The steepest descent algorithm partitions all flow from pixel j to the most downhill neighboring cell. In contrast, the MFD algorithm disperses flow to all downslope neighboring pixels, proportional to the slope S_i, which is the slope between pixel j and neighbor i. We refer to the fraction of flow passed from j to a neighbor pixel i as "Influence" I_i. We calculate I_i as

$$I_i = \frac{S_i^p}{\sum\limits_{k=1}^{n} S_k^p}. \tag{2}$$

In Eq. 2, n denotes the total number of downslope neighbors of j (which varies in space) and p is an empirical exponent. Multiple j-locations may contribute to I_i. Freeman (1991) found that $p = 1.1$ produces flows that are least influenced by gridding.

An advantage of MULTIFLOW is that it only requires the flow algorithm to be run once and the results are deterministic. DOWNFLOW (Favalli et al. 2005), a similar lava flow model

Table 2 Parameters for the example lava flows shown in Fig. 3

Example Flow	a	b	c
F1	1	1	5
F2	0.1	1	5
F3	1	1	10
F4	0.1	1	10
F5	1	0.75	10
F6	1	2	30
F7	0.1	2	30
F8	1	1	30

that utilizes the steepest descent algorithm to predict flow routing, performs thousands of steepest descent calculations on stochastically perturbed topography in order to generate laterally dispersed flow paths. However, both algorithms are quite efficient (on the order of ~ 1 s for typical DEMs).

We use the MFD algorithm supplied with Topotoolbox (Schwanghart and Kuhn 2010), which is run in Mathworks MATLAB software. Because the MFD algorithm is the most dispersive of commonly employed drainage algorithms (Tarboton 1997), we apply a threshold to limit the dispersivity and flow extent. This thresholding approach is similar to some other lava flow routing models (e.g., Ishihara et al. 1990;
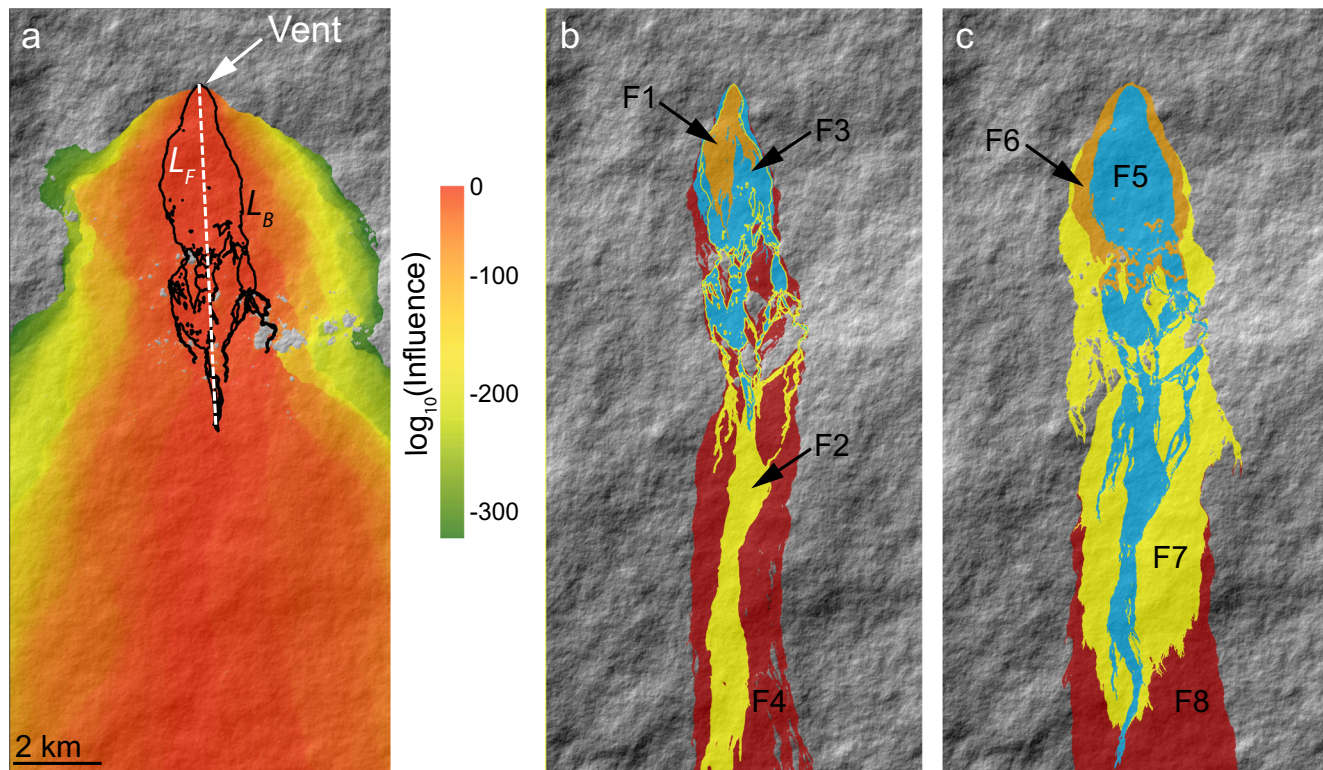

Fig. 2 a Shaded relief map overlaid with a color map of influence produced by MUTLIFLOW. The internal and perimeter flow boundaries (Pi in Eq. 5) are shown in black. The dashed white line shows the length used to calculate $Lmax$ in Eq. 5. The flow was routed across randomly produced, red noise topography. Shaded relief of the same topography with **b** example flows F1-F4 and **c** example flows F5–F8 produced by applying different thresholds to the influence in panel **a**. Outline of F2 and F6 is shown as the flow boundary near the vent is obscured by the other flows. See Table 2 for corresponding parameters a, b, c of Eq. 3

Young and Wadge 1990; Crisci et al. 2004). We define a dimensionless threshold function T_I on the Influence field I_i (Eq. 2) that takes the form

$$T_I = aL^b - c, \qquad (3)$$

where L is the horizontal distance from the vent as measured from a scaled map. a, b, and c are empirically-tuned parameters (a has units of length^{-b} while b and c are dimensionless). We include all locations contiguous to the vent where $I_i > T_I$. In Fig. 2, we show eight simulated flows chosen to highlight the effect of different threshold parameters. At a pixel where calculated Influence is equal to 1, the predicted percentage of lava flow paths crossing that point is 100%. This only occurs at pixels identified as vents where flow routing starts. As Influence decreases from 1, the likelihood of lava flowing across that pixel decreases. Thresholding the Influence field is a parameterization of physics that limit the extent to which a flow can access all possible downslope pathways.

A simple expectation of how the threshold parameters (a, b, and c in Eq. 3) impact flow geometry is not always possible, because substrate topography has a significant role for potential flow paths. However, the MFD routing Eq. 2 provides some intuition of how the threshold parameters influence flow geometry. c is a uniform threshold for I_i, and will generally define a contour that is longer in the downslope versus cross-slope direction (Fig. 2, parameters listed in Table 2). Increasing a or decreasing b preferentially weights the downslope direction mapped by L and produces longer flows with modest increases in flow width.

Other forms of the threshold function are possible, for example including local gradient, gradient over some flow distance, or a combination of gradient and L. Thresholding may also be viewed as a platform for incorporating auxiliary models for flow volume and lava rheology (e.g., Ishihara et al. 1990; Wadge et al. 1994; Crisci et al. 2004), which might be time-dependent. Here we focus our attention on Eq. 3 as a simple threshold that is able to reproduce real and continuously connected lava flow pathways.

Combining the multiple flow direction algorithm with spectrally filtered topography to model lava flows

One disadvantage of a purely flow-routing approach to lava flow prediction is the sensitivity of flow-routing algorithms to small-scale roughness in DEMs. Any sign change in slope will divert predicted flow, meaning that DEM noise as well as small obstacles that would be overtopped by real flows will contaminate results. We solve this problem by applying a low-pass filter to DEMs as a pre-processing step before calculating a flow path. Because topographic height varies systematically as a function of wavelength in volcanic landscapes (Fig. 1), low-pass filtering provides a proxy for finite flow thickness by removing small roughness elements. This is preferable to simply downsampling DEM resolution because spectral filtering provides more precise control on roughness as a function of wavelength. We utilize a Fourier domain approach, but other spectral methods such as those using wavelets or Slepian basis functions (Simons 2009) could equally well be used.

With this spectral filtering step, we are now in a position to test MULTIFLOW against observations. In what follows, we calibrate the model using the three test cases previously discussed. A MULTIFLOW run involves three steps, once a DEM has been chosen and vent location pixel(s) identified. First, we low-pass filter the DEM to remove high-frequency roughness/noise. Second, we apply the MFD algorithm (Eq. 2) to produce an Influence field map I_i of all possible flow pathways. Finally, we threshold I_i via Eq. 3 to produce a synthetic lava flow. To find the closest match with real lava flows, we complete a parameter space search of a, b, and c from Eq. 3 and consider a range of low-pass filter cutoffs to maximize fits with known flow outlines.

Quantifying lava flow morphology with Jaccard Index and Branching Index

We use the Jaccard similarity index (J_s) (Levandowsky and Winter 1971) to assess how well our modeled lava flows match real flows (Fig. 3). The similarity index J_s is a Boolean measure of similarity between two pixel sets A and B, defined as

$$J_s(A, B) = \frac{|A \cap B|}{|A \cup B|} \qquad (4)$$

and takes values between zero and one. A value of one is a perfect match and a value of zero indicates that there is no overlap between the modeled flow and the real flow. Other models (e.g., Favalli et al. 2009; Kubanek et al. 2015; Cordonnier et al. 2016) have used this metric (sometimes labeled a "fitness index") to compare simulated lava flow pathways with the pathways of real flows. Fundamentally, J_s compares the overlapping area of the modeled flow and the real flow to the combined area of the modeled flow and real flow.

We also investigate how well our model reproduces lava flow branching, using a metric that we refer to as the branching index (b_i). We calculate the branching index as the sum of all internal and external (perimeter) boundary contour lengths P_i of the flow divided by the maximum horizontal distance L_{max} of the vent to the farthest flow lobe (a measure of total flow length for a straight flow),

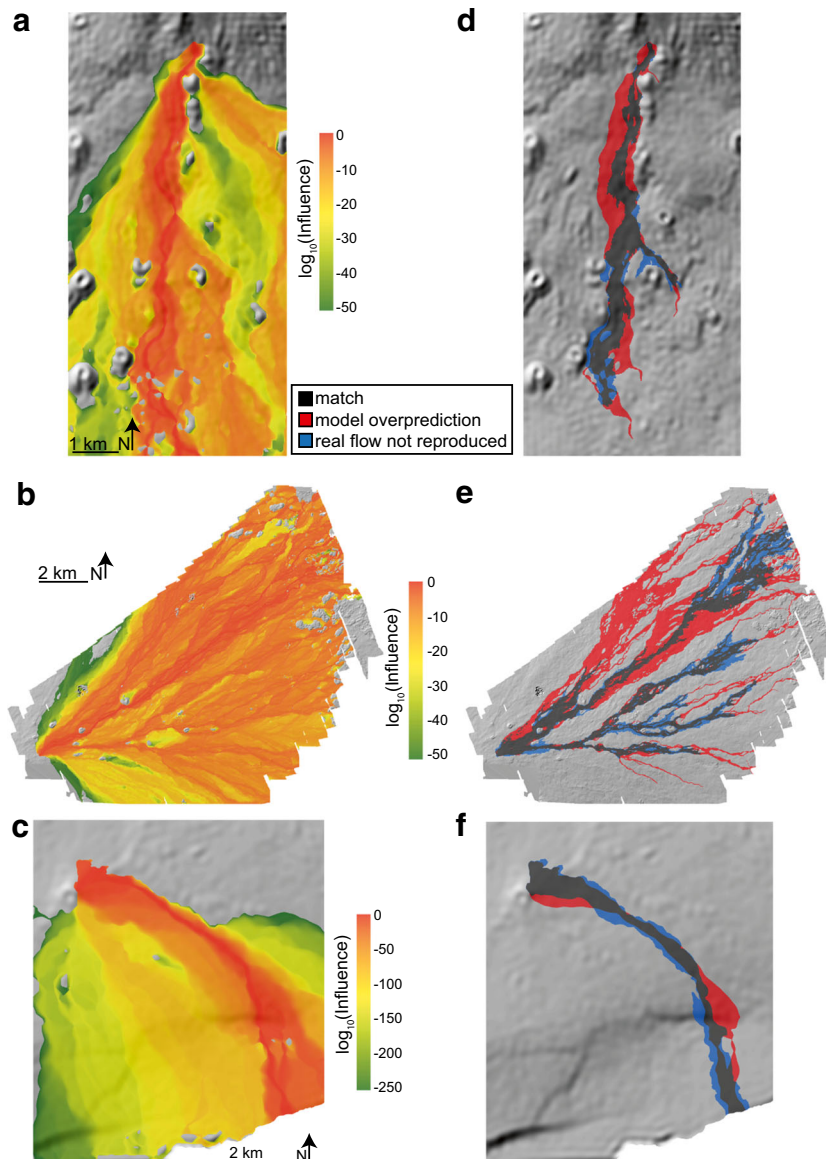$$b_i = \frac{1}{L_{max}} \sum_{i=1}^{N+1} P_i \qquad (5)$$

Fig. 3 Shaded relief maps of **a** the region encompassing the 2001 Mt. Etna lava flow of interest with color map showing where $\log_{10}(\text{influence}) > -50$, which accounts for 92% of the influence values, **b** the region encompassing the 1984 Mauna Loa lava flow of interest with color map showing where $\log_{10}(\text{influence}) > -50$, and **c** the region encompassing the 2011 Kīlauea flow of interest with color map showing where $\log_{10}(\text{influence}) > -250$. For both Mauna Loa and Kīlauea, the influence maps show 97% of the influence values. **d–e** Shaded relief maps of the respective regions with color map comparing the results of the best-fit J_s flow produced with MULTIFLOW and the flow of interest

where N is the topological genus of the flow outline (the number of internal boundaries or holes). In the case of $N = 0$, P_i is the length of the flow perimeter and there are no internal boundaries. In all cases, the summation of P_i can be considered as the total length of all flow boundaries, which includes both the perimeter and internal boundaries. The branching index for case studies here reflects visual inspection of flow outlines, with $b_i = 19.2$ Mauna Loa flow and $b_i = 3.5$ and $b_i = 4.5$ for Kīlauea and Etna, respectively (Table 4).

This index is comparable to other recently proposed metrics of lava flow dispersivity. The "perimeter factor" of Rumpf et al.

(2018), for example, compares the ratio of flow perimeter divided by flow area to the same ratio computed for an ellipse with length and width equal to the maximum length and width of the flow. As a purely geometrical analogy, for a circular flow on a flat plane with the vent on the perimeter, $b_i = \pi$ while the perimeter factor is unity. Parameter b_i is thus designed to integrate anabranching structures internal to the total flow outline and will diverge from the perimeter factor for complicated flow outlines. The "dispersivity index" of Favalli et al. (2012) is derived from the stochastic procedure of DOWNFLOW, measuring the statistical tendency for an envelope of many steepest

descent pathways to vary laterally. It is based upon a different flow routing scheme and requires secondary thresholding of steepest descent pathways so is not directly comparable to b_i, but we expect that the dispersivity index is sensitive to the same topographic characteristics.

Results

Calibration and model applications

We first test MULTIFLOW against the Lower Fissure System 1 lava flow from Mt. Etna's 2001 eruption (Fig. 3), iteratively refining parameter grid searches for the parameters in Table 3 until J_s is maximized for the finest increment investigated. We find a maximum value of $J_s = 0.49$ and $b_i = 4.6$, giving an excellent match to b_i of the real flow. The best-fit parameters are reported in Table 4.

We repeat the same analysis for Mauna Loa and Kīlauea (Fig. 3). For Mauna Loa, we route flow across the pre-flow DEM starting at the maximum elevation of the DEM near the vent. We use a different filter and find that a low-pass filter $F_L = F_H/1.5$ minimizes edge effects. For Kīlauea, MULTIFLOW spreads lava across two distinct pathways: one to the northeast and one to the southeast. However, the Peace Day vent only produced significant flow to the southeast (Fig. 1c). The area to the northeast of the peace day vent is lava flows that occurred from 1983 to 1986 (Sherrod et al. 2007) which flowed into a forest ~2 km from the vent. We limit the extent of this flow path and focus on matching the flow path to the southeast. This artificially inflates our estimate of J_s.

For all three test cases, we complete a parameter search for the parameters that maximize J_s (Tables 3 and 4). The resulting values of J_s are 0.37 for Mauna Loa, 0.54 for Kīlauea, and 0.49 for Mt. Etna. The maximum J_s is found for a low-pass filter threshold that removed topography with wavelengths below 50 m (F_H) for Mauna Loa, 270 m for Kīlauea, and 130 m for Mt. Etna. We do not systematically analyze the misfit space for these cases, but do note that particularly in the case of Kīlauea, similar maxima in J_s are achieved for other filter thresholds. In general, J_s is maximized for filters in the range of 10s to ~100 m. In Fig. 4, we show the resulting influence flow paths for low-pass filters with different wavelengths for Mauna Loa. We measure the branching index for the real flow and the best-fit modeled flow and report the results in Table 4.

Lava flows on synthetic topography

To generalize our case studies, we complete two numerical experiments using synthetic topography for the Hawaiian flows. In the first experiment (Fig. 5), we route lava on synthetic DEMs with different spectral characteristics (topographic variance and spectral slope) and investigate how b_i varies.

In the second experiment, we reproduce synthetic landscapes that have the same topographic variance and spectral slope as the Mauna Loa and Kīlauea flow regions. We then route lava using MULTIFLOW across the landscape and compare the resulting values of b_i with the values from the 1984 Mauna Loa flow and 2011 Kīlauea flow.

We create synthetic landscapes by varying two characteristics—topographic variance and spectral noise. Other morphological characteristics are not reproduced, such as complexity associated with fluvial river channels or volcanic landform features (e.g., cones, tumuli, flow boundaries). We view these numerical experiments as establishing a null model from which the influence of specific processes can be reliably quantified.

For the first experiment, we create synthetic landscapes with dimensions of 6×7 km and grid size of 10 m. We create topography that has the same underlying slope (5.1°) as Mauna Loa, MULTIFLOW threshold parameters (a, b, c) and spectral filter cutoff (50 m) (Table 4). We route lava from a vent location 1.5 km from the top boundary and centered in the x-dimension (Fig. 5b–j). This allows the flow to disperse toward the top of the grid before the slope ultimately influences the flow direction and steers it toward the lower boundary. We limit the influence of edge effects by cropping the grid to a final width of 5 km in the x-direction and 6 km in the y-direction, which allows for a flow length of ~5 km. For each variance and spectral slope, we complete 10 model runs to find an average b_i. Results are summarized in Fig. 5a.

The resulting values of b_i for the lava flows routed over synthetic topography are comparable to the values we measured at Mt. Etna, Kīlauea, and Mauna Loa for the real lava flows. The results suggest that landscapes with both low spectral slope and variance (Fig. 5a), for which the roughness amplitude is more uniform at all scales, should produce high degrees of branching. Branching index b_i remains high for a particular combination of variance and spectral slope (Fig. 5a).

For the second experiment, we compare b_i for lava flows routed across synthetic landscapes with the same topographic variance and spectral slope as Mauna Loa and Kīlauea (Table 4). We complete a hundred model runs with synthetic topography. For the topography that matched Mauna Loa's spectral characteristics and best-fit MULTIFLOW parameters, b_i is 8.24 ± 0.39 (mean ± standard error), which is 46% less than the b_i measured for the 1984 Mauna Loa flow measured within a 5×5-km window and 31% less than the flow predicted by the MULTIFLOW routed on the pre-flow Mauna Loa DEM measured inside a 5×5-km window. For the synthetic topography with Kīlauea's spectral characteristics and best-fit MULTIFLOW parameters, b_i is 5.79 ± 0.21, which is 70% higher than b_i for real Kīlauea within a 5×5-km window and 81% higher than the flow predicted by MULTIFLOW routed on the pre-flow Kīlauea DEM measured inside a 5×5-km window.

Table 3 Considered
DOWNFLOW parameters

	Range	Finest increment explored
Low-pass filter cutoff, $1/F_H$ (1/m)	20–1000	10
Coefficient (a)	1–50 and 1/(1–50)	1
Exponent (b)	0.5–4	0.1
Intercept (c)	1–50	1

Discussion

Assessing and mitigating volcanic hazards relies on accurately predicting lava flow planform shape (Richter et al. 2016; Poland et al. 2016). We have focused on the role of topography on flow pathways, implementing and testing a new flow routing algorithm and exploring the role of spectral analysis both for forecasting flow paths and quantifying the role of landscape roughness at a range of scales. Our approach should be considered distinct from, and not a replacement for, physics-based flow models. We see the MULTIFLOW model and others like it (e.g., Harris 2013; Cappello et al. 2016; Chevrel et al. 2018; de' Michiele Vitturi and Tarquini 2018) as a framework for integrating parameterized physics with highly efficient treatments of rough topography. Throughout the discussion section, we assess the applicability of MULTIFLOW to real flows in the context of our synthetic landscape parameter study. We end with an examination of the Island of Hawaiʻi as an example of how complexities on larger scale volcanic landscapes can be explored using tools introduced here.

MULTIFLOW predicted flow pathways, branching, and time evolution

An attractive characteristic of this model is that it is both efficient and easy to implement: a single model run produces dispersive flow pathways while a threshold function is easily calibrated from real flows. Parameterization of yielding behavior and effusion rate-related effects has not been undertaken here but are an obvious place to incorporate known physics. Rule-based flow models generally must deal with flow paths that are sensitive to grid resolution, which sets the gradient between neighboring pixels. By applying a spectral filter as done here (i.e., recognizing that short wavelength features are generally not important for flow routing), grid resolution will have less influence on the results. This feature of our modeling framework is demonstrated in Fig. 4 for the Mauna Loa flow, where different low-pass filter wavelengths F_L are a proxy for DEMs of varying resolution.

When calibrated, MULTIFLOW produces a J_s for the community benchmark of the 2001 Etna flow (Coltelli et al. 2007) that is comparable to both rules- and physics-based models. Parameter J_s evaluated for four different rules- and physics-based models ranges from 0.16 to 0.63 (Cordonnier et al. 2016), while J_s for MULTIFLOW is 0.49. Applied to lava flows from Mauna Loa and Kı̄lauea, this model is also able to reproduce flow branching and length with minimal tuning. However, b_i exhibits some dependence on spatial scale for which it is measured. This is especially true for Mauna Loa, which continues to branch as distance from the source increases. Thus, b_i increases with the spatial scale for which it is measured for this flow.

For all three cases, our modeled values of b_i were within a factor of two of the real flows while a factor of five difference is observed between the observed Mauna Loa and Kı̄lauea flows (Table 4), which suggests that tuning MULTIFLOW captures many of the processes that influence branching. Although we cannot specifically identify all physical factors that drive differences in branching between flows in addition to substrate roughness, time evolution of flow pathways is one likely contributor. For example, the 1984 Mauna Loa flow was relatively short-lived compared to the 2011 Kı̄lauea flow. We expect that b_i will increase with time at early stages of an eruption. But at later times flow pathways may converge, for example through filling in new topographic lows created by the flow (for example kipukas that begin as topographic highs but become lows as the flow progressively builds topography). This reduces flow planform perimeter relative to length, so b_i would decrease through time.

Although a model for time variation of flow behavior is left for future work, we have shown that tuning MULTIFLOW parameters can reproduce the resulting planform patterns in diverse emplacement scenarios. Topographic roughness is likely convolved with time-evolution of long-lived lava flows: branching will increase with time initially as the flow accesses pathways that are defined by pre-eruptive topographic roughness, but modification of topography by progressively longer-lived flows may decrease branching. Long-lived pahoehoe flows advance and widen via inflation and break-outs (e.g., Walker 1971; Hon et al. 1994; Cashman et al. 1999), versus ʻaʻā flows that may widen due to overflows arising from blockages or surges (e.g., Kilburn 1981; Lipman and Banks 1987; Guest et al. 1987). As a result, flow style could also be reflected in b_i. Such processes could be better disentangled with co-eruptive multi-temporal DEM generation, such as is increasingly possible with repeat LiDAR and drone-based photogrammetry (Dietterich et al. 2018).

Shorter-lived flows should be more significantly influenced by topography, as suggested by our flow routing analysis. However, a weakness of MULTIFLOW is its inability to

Table 4 Best-fit parameters and results

	Mauna Loa	Kīlauea	Mt. Etna
Low-pass filter cutoff (m)	50	270	130
Coefficient (a)	1/4	3	1/33
Exponent (b)	0.9	0.7	3.0
Intercept (c)	8	28	10
Jaccard similarity, J_s	0.37	0.54	0.49
Overlapping area (km^2)	13.92	5.48	1.64
Flow area not reproduced (km^2)	5.63	2.57	0.37
Over predicted flow area (km^2)	18.10	2.16	1.32
b_i real flow	19.2	3.5	4.5
b_i 5 × 5 km real flow	15.2	3.4	4.8
b_i best-fit MULTIFLOW flow	37.8	3.6	4.6
b_i 5 × 5 km best-fit MULTIFLOW flow	11.9	3.2	4.0

reproduce features such as blockages along the Mauna Loa flow, which caused outbreaks to form that created new channels and expanded the geometry (Lipman and Banks 1987; Dietterich and Cashman 2014). For Mauna Loa, our model predicts significant flow on the northern edge of the existing flow path, suggesting an important role for flow dynamics (establishment of a stable flow path, and perhaps vent geometry) in influencing the actual lava flow paths. For Kīlauea, we limited flow to the north. However, we find it likely that all existing lava flow models would also route significant quantities of lava to the north erroneously if the same pre-eruptive

DEM were used. This highlights the challenges of using models to reproduce specific flow paths in the face of poorly constrained physical processes (rupture of lava flow crust that generates break outs), and also emphasizes the importance of accurate DEMs (e.g., Tarquini and Favalli 2011; Harris 2013; Richter et al. 2016; Poland et al. 2016).

Flow thickness in MULTIFLOW

The MULTIFLOW model does not explicitly calculate flow thickness. However, thickness may be semi-quantitatively
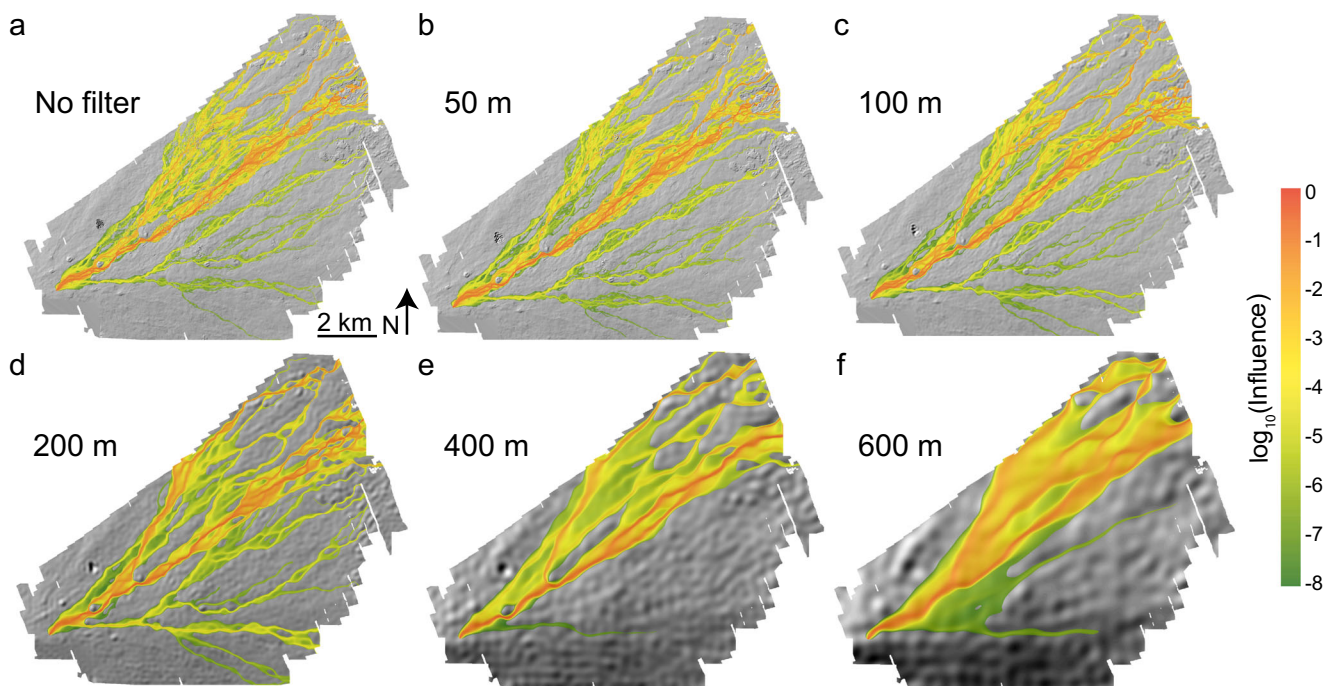

Fig. 4 **a–f** Shaded relief maps of region near the 1984 Mauna Loa, HI flow for landscape with different low-pass filters overlaid with color maps of influence produced by the MUTLIFLOW lava flow model. We limit the flows according to the best-fit parameters for the threshold function in

Table 4. The low-pass filter wavelength cutoff ($1/F_H$) is noted next to the shaded relief in each panel except for **a** where we show the unfiltered results
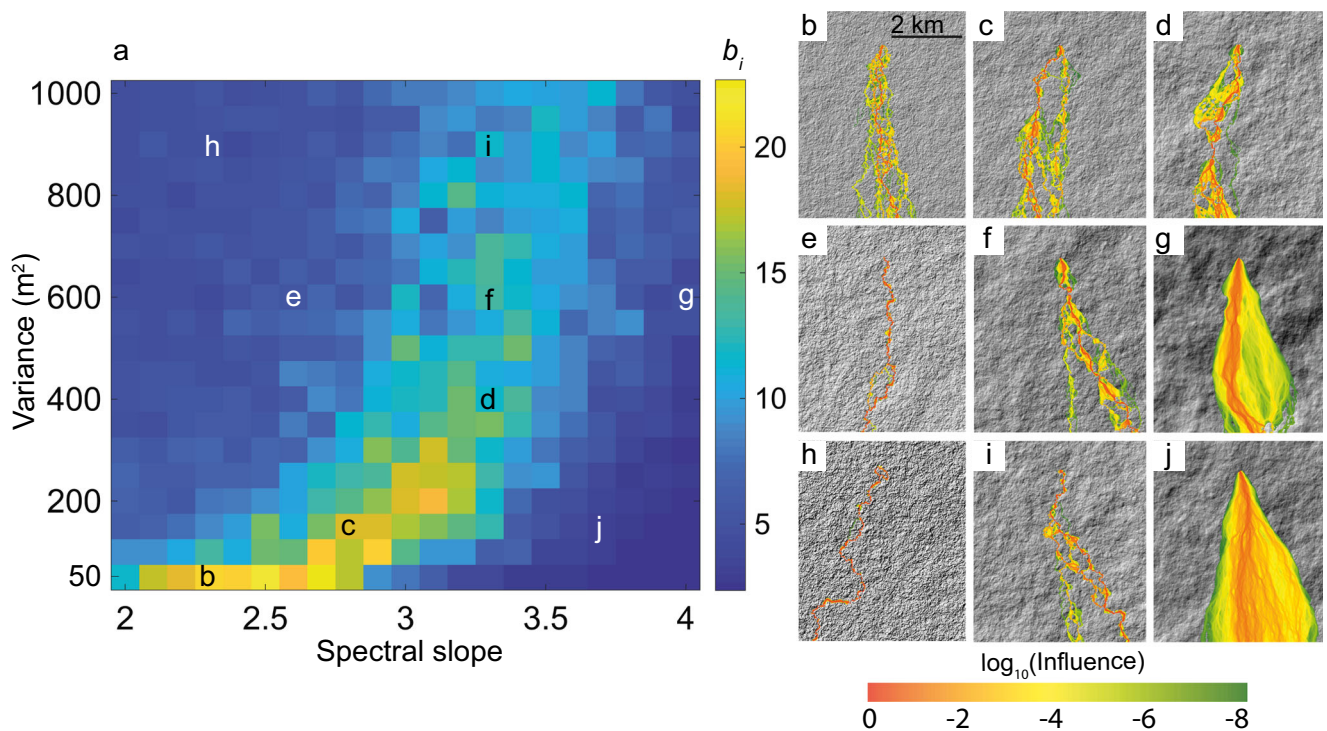
Fig. 5 **a** Regime diagram showing the branching index (b_i) for MULTIFLOW results for synthetic landscapes with different spectral characteristics. Each pixel is the average b_i for 10 model runs. We used the best-fit calibration values for Mauna Loa for the threshold function (Table 3) and the background slope (5.14°). Letters correspond to panels **b–j**. **b-j** Shaded relief maps overlaid with color maps of influence produced from MULTIFLOW highlighting results from panel **a**. Examples show the model run for the b_i that most closely matches the mean b_i at each location in **a**

estimated by the low-pass filtering of pre-existing topography. As topography is smoothed, flow paths and divergence of influence decrease, so branching index b_i decreases (Fig. 4). Taken as a metric of substrate influence alone, this suggests that small scale features with wavelengths < 130 m for Mt. Etna, < 50 m for Mauna Loa are unimportant for influencing the flow paths. Because features of low vertical amplitude are inundated by flows, the spectral filter wavelength is a measure of flow thickness through Eq. 1, although translating wavelengths directly to vertical thickness is complicated by topographic overlap in frequency bins (Perron et al. 2008).

Thickness assessed this way is similar to the approach Favalli et al. (2005) who use stochastic perturbation of topography to produce ensembles of steepest descent pathways that match observations. The spectral technique is more systematic because topographic amplitude associated with features of a given wavelength is given directly by the power spectral density (Fig. 1). However, as discussed in the previous section, time evolution of flow pathways likely modifies initial substrate roughness for long-lived flows. For the Kīlauea case, we suspect that the large low-pass filter cutoff (wavelengths < 270 m) required to maximize MULTIFLOW fit is a reflection not solely of pre-eruptive topography but also the construction of a flow field and topographic modification during a multi-month

effusive event. Artifacts arising from high-frequency DEM noise may also play a role in this model result for Kīlauea.

We can use real observations to compare with thicknesses assessed from MULTIFLOW. The analysis of the Mauna Loa flow by Dietterich et al. (2015) demonstrates that average flow thicknesses are best correlated to slope when averaged over 70–90 m (their Fig. 22.17). Spatial averaging with a moving window is equivalent to low-pass filtering. Thus, the result of Dietterich et al. (2015) both confirms our independent flow routing analysis of this DEM, and suggests that the 1–5 m height roughness is associated with our best fitting ~ 50-m wavelength low-pass filter cutoff. This can also be inferred from the power spectra in Fig. 1 as a proxy for flow thickness.

MULTIFLOW model results for Kīlauea, Mauna Loa, and Mt. Etna imply that coarse resolution (~ 10 s m) DEMs may be suitable for lava flow routing as unresolved features do not play a significant role in determining large-scale lava flow pathways. This is important for areas that do not have existing high-resolution DEMs available. Misfit of best-fitting MULTIFLOW models also suggests that finer scale analysis of lava flow breakouts, tubes, and channels require higher resolution data and field observations, and probably a different modeling framework.

Lava flow experiments on synthetic topography

Our parameter study provides a qualitative guide for how systematic changes in red noise characteristics of the substrate influence flow branching. The degree of branching exhibits a well-defined local maxima variance and spectral slope space (Fig. 5a), which can be understood as a consequence of the degree of connectivity between neighboring downslope pixels. The degree of "redness" encapsulated by spectral slope β trades off with variance to produce the maximum branching: past the self-similar value of $\beta = 3$, larger variance at a given β is required to most efficiently divert flow pathways, due to the decreasing width-height ratios of smaller wavelength substrate roughness. $\beta < 3$ exhibits smaller width-height ratios for smaller wavelengths, meaning that small obstacles are more likely to divert the flow.

In reality, finite flow thickness (not accounted for in Fig. 5) places a lower bound on the variance that can affect flows, while gravity places a lower bound on β: short wavelength, large amplitude structures do not persist in real landscapes (Fig. 1). The volcanic landscapes that we analyzed do not clearly exhibit the steeper spectral slope at high frequencies seen in other landscapes (Perron et al. 2008), which may indicate that smaller scale topographic features are taller than they are in erosional settings. This could result from a lack of diffusive erosional processes such as hillslope creep in young volcanic landscapes.

We do not directly compare the parameter study in Fig. 5 to Kīlauea and Mt. Etna because the underlying slope is fixed in this experiment to the slope of Mauna Loa. The large variance seen at Mt. Etna is outside the range of our parameter study, but arises from physical constructs (cinder cones that have heights in the range of ~100 m, Karlstrom et al. 2018). We anticipate that as background slope increases flow paths may become more continuous as neighboring pixels become more connected. However, flow thickness also likely decreases as background slope increases (Dieterich and Cashman 2014), which would tend to increase branching. Such tradeoffs are well-captured by a flow routing model such as MULTIFLOW.

Spectral analysis as a tool for quantifying lava flows

Our experiments with real flows and synthetic red-noise surfaces suggest that multi-scale topography plays a first-order role in controlling lava flow paths and branching. This suggests that understanding controls on the distribution of topographic roughness in volcanic areas may improve understandings of lava flow morphology. Investigation of synthetic landscapes (such as in Fig. 5) helps develop intuition for the topographic features that are required to reproduce the degree of branching that we see in lava flows. But we can also examine real volcanic landscapes to identify processes that shape topography in a systematic way, which could lead to deviations from ideal red noise spectra and contribute variance to specific frequency bands. Identification of such commonalities in landscapes could help lava flow forecasting, for example by guiding the choice of low-pass filter cutoff used to implement MULTIFLOW or to assess the resolution of DEM needed to predict flows.

We illustrate this approach by comparing the topographic power spectra for different regions of the Island of Hawai'i (Fig. 6) containing basaltic lava flows that range in age from 0 to ~750 ka (Trusdell et al. 2005; Sherrod et al. 2007). Following Perron et al. (2008), we normalize the topographic power spectrum by dividing the spectra of each region of interest by the spectra for a young volcanic landscape that is devoid of pronounced volcanic features or geomorphic response.

Young volcanic landscapes often have low variance (for example, the flank of Mauna Loa shown in Fig. 6g) and when the power per frequency is normalized, spectral anomalies relative to such young surfaces become more apparent. As Hawaiian volcanic landscapes age past ~100 ka, spectral peaks associated with wavelengths of ~50 to 500 m become discernable as high normalized power (Fig. 6h). This corresponds to development of fluvial channels on lava flows of increasing age. Even the degree of channel incision appears to be reflected in the normalized periodograms with more deeply incised channels producing higher normalized power for frequencies associated with channel incision (Fig. 6). Such systematic variability in landscape roughness should lead to systematic variations in lava flow branching (Fig. 5).

Beyond lava flow forecasting, spectral analysis provides a tool to place volcanic landscape evolution and lava flow emplacement in the context of other Earth systems. Climatic influence on erosion rates and channel incision efficiency (Ferrier et al. 2013b; Murphy et al. 2016) has been demonstrated for the Hawaiian Islands, but the role of lava flow age is less clear. Figure 6 points to a unique opportunity for studying the temporal evolution of channel incision on volcanic landscapes. Young lava flows are characterized by high infiltration rates, limited channel dissection (Lohse and Dietrich 2005) and springs (Whiting and Moog 2001) that help drive consistent discharge due to availability of groundwater. As lava flows, age, physical, and chemical weathering decrease infiltration, leading to surface runoff and eventually channel incision that increases with time.

In Fig. 6, volcanic landforms such as monogenetic cones are also apparent, and their mean size is reflected in the spectral peak around ~1 km in the normalized periodogram. This range is consistent with distributions of cinder cones worldwide (Karlstrom et al. 2018), and suggests that other volcanic landform types with well-defined size distributions could be identified using spectral analysis.
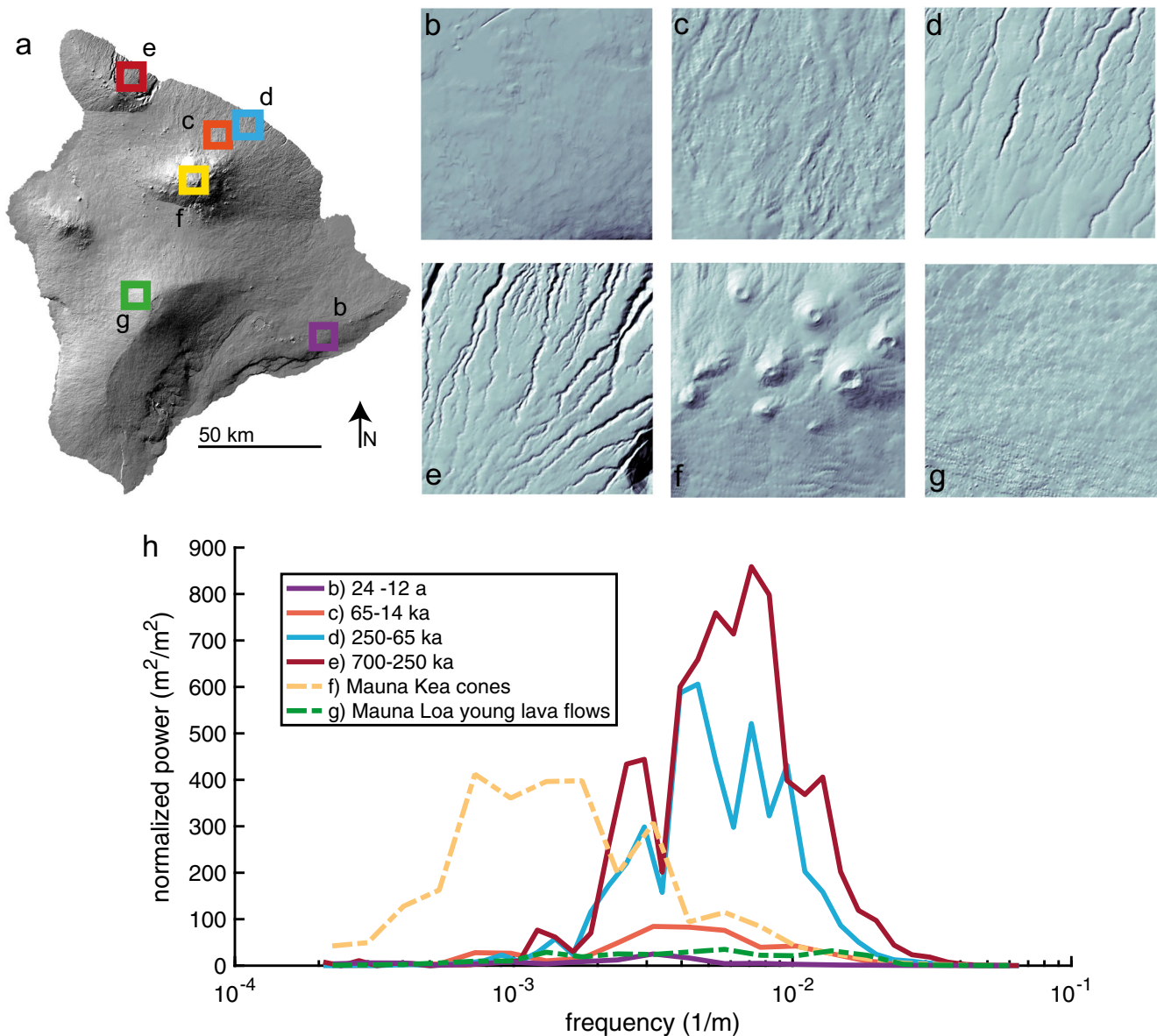
Fig. 6 a Shaded relief map of the Island of Hawaiʻi created from 30 m DEM with regions of interest outlined (gis.ess.washington.edu/data/raster/thirtymeter/bigisland/index.html). Letters correspond to shade relief maps in panels **b**–**g** and results shown in panel **h**. **b**–**g** Shaded relief maps for regions of interest in panel **a**. **h** Normalized periodogram of the regions in panels **b**–**g**. For each region, spectral power is normalized by the spectral power of the young lava flows (1–1.5 ka) on the flank of Mauna Loa

These two examples (channel incision and cinder cones) illustrate how volcanic landscape form encodes process. In combination with regime diagrams such as Fig. 5 that associate spectral characteristics of the landscape with flow branching, understanding such longer-term controls on topography may lead to better characterization and forecasting of lava flow pathways. Of course, the converse is also true: construction of topography by volcanic processes such as lava flows can have a spatially extensive and long-lasting impact on landscape erosion patterns (Busby et al. 2008; O'Hara et al. 2019). Better constraints on lava flow morphology are needed

to deconvolve competing influences on landscape evolution in volcanic settings.

Conclusion

We introduced a new lava flow path simulator (MULTIFLOW) that utilizes the multiple flow direction (MFD) routing algorithm in conjunction with a thresholding function. When combined with a spectral filtering step and calibrated empirically, MULTIFLOW reproduces lava flows with a similar degree of

branching, area, and length as seen for three test flows at Mt. Etna, Mauna Loa, and Kīlauea. Furthermore, analysis of the spectral characteristics of these three volcanic landscapes demonstrates that topographic variance and spectral slope can characterize the multiscale topographic roughness that influences lava flow morphology. Through a series of numerical experiments, we showed that spectral slope and variance influence the degree to which lava flows branch.

Future work could minimize the number of parameters required to calibrate MULTIFLOW for a given prediction scenario by incorporating temperature- and shear-rate-dependent rheology parameterized from field and laboratory data (e.g., Robertson and Kerr 2012; Soldati et al. 2016; Kolzenburg et al. 2016) and connect flow routing pathways to known eruption volumes (Young and Wadge 1990; de' Michiele Vitturi and Tarquini 2018). Such additions to the model are also likely to generate additional avenues to produce branching flows. Lastly, we showed that in one natural setting, on the Island of Hawai'i, spectral characteristics vary systematically with age of the surface. Properly calibrated, such systematic variations suggest that flow morphology and branching might be a priori predicted given DEMs with sufficient accuracy, especially if DEMs can be updated through time as lava modifies pre-existing topography. Spectral analysis might also aid volcanic hazard assessment, by constraining the dimensions of natural or man-made objects that lava flows are sensitive to and the range of possible pathways available to flows (Favalli et al. 2009).

Code availability   The MULTIFLOW lava flow routing model is available on GitHUB at https://github.com/leifkarlstrom/MULTIFLOW_lava_flow_model.git and VHub. DEM spectral analysis tools developed by J.T. Perron may be obtained at http://web.mit.edu/perron/www/downloads.html.

References

Applegarth LJ, Pinkerton H, James MR, Calvari S (2010) Morphological complexities and hazards during the emplacement of channel-fed `a`ā lava flow fields: a study of the 2001 lower flow field on Etna. Bull Volcanol 72:641–656. https://doi.org/10.1007/s00445-010-0351-1

Behncke B, Neri M (2003) The July–August 2001 eruption of Mt. Etna (Sicily). Bull Volcanol 65:461–476. https://doi.org/10.1007/s00445-003-0274-1

Bilotta G, Hérault A, Cappello A, Ganci G, Del Negro C (2016) GPUSPH: a smoothed particle hydrodynamics model for the thermal and rheological evolution of lava flows. Geol Soc Lond, Spec Publ 426(1):387–408

Busby CJ, DeOreo SB, Skilling I, Gans PB, Hagan JC (2008) Carson Pass-Kirkwood paleocanyon system: paleogeography of the ancestral cascades arc and implications for landscape evolution of the Sierra Nevada (California). Geol Soc Am Bull 120(3/4):274–299

Cappello A, Hérault A, Bilotta G, Ganci G, Del Negro C (2016) MAGFLOW: a physics-based model for the dynamics of lava-flow emplacement. Geol Soc Lond, Spec Publ 426(1):357–373

Cashman KV, Thornber C, Kauahikaua JP (1999) Cooling and crystallization of lava in open channels, and the transition of Pāhoehoe lava to 'A'ā. Bull Volcanol 61:306–323. https://doi.org/10.1007/s004450050299

Cashman KV, Soule SA, Mackey BH, Deligne NI, Deardorff ND, Dietterich HR (2013) How lava flows: new insights from applications of lidar technologies to lava flow studies. Geosphere 9:1664–1680. https://doi.org/10.1130/GES00706.1

Chevrel MO, Labroquère J, Harris AJ, Rowland SK (2018) PyFLOWGO: an open-source platform for simulation of channelized lava thermo-rheological properties. Comput Geosci 111:167–180

Coltelli M, Proietti C, Branca S et al (2007) Analysis of the 2001 lava flow eruption of Mt. Etna from three-dimensional mapping. J Geophys Res 112:F02029. https://doi.org/10.1029/2006JF000598

Cordonnier BJR, Lev E, Garel F. (2014), "BENCHMARKING LAVA FLOWS -BM5 - ETNA 2001," https://vhub.org/resources/3454

Cordonnier B, Lev E, Garel F (2016) Benchmarking lava-flow models. Geol Soc Lond Spec Publ 426:425–445. https://doi.org/10.1144/SP426.7

Crisci GM, Rongo R, Di Gregorio S, Spataro W (2004) The simulation model SCIARA: the 1991 and 2001 lava flows at Mount Etna. J Volcanol Geotherm Res 132(2–3):253–267

Crisp J, Cashman KV, Bonini JA, Hougen SB, & Pieri DC. 1994. Crystallization history of the 1984 Mauna Loa lava flow. Journal of Geophysical Research, B99, 7177–7198.

Crozier J, Karlstrom L, Yang K (2018) Basal control of supraglacial meltwater catchments on the Greenland Ice Sheet. Cryosphere 12:3383–3407

de' Michiele Vitturi M, Tarquini S (2018) MrLavaLoba: a new probabilistic model for the simulation of lava flow as a settling process. J Volcanol Geotherm Res 349:323–334

Deardorff ND, Cashman KV (2012) Emplacement conditions of the c. 1, 600-year bp collier cone lava flow, Oregon: a LiDAR investigation. Bull Volcanol 74:2051–2066. https://doi.org/10.1007/s00445-012-0650-9

Del Negro C, Fortuna L, Herault A, Vicari A (2008) Simulations of the 2004 lava flow at Etna volcano using the magflow cellular automata model. Bull Volcanol 70(7):805–812

Deligne NI, Cashman KV, Roering JJ (2013) After the lava flow: the importance of external soil sources for plant colonization of recent lava flows in the Central Oregon cascades, USA. Geomorphology 202:15–32. https://doi.org/10.1016/J.GEOMORPH.2012.12.009

Dietterich HR, Cashman KV (2014) Channel networks within lava flows: formation, evolution, and implications for flow behavior. J Geophys Res Earth Surf 119:1704–1724. https://doi.org/10.1002/2014JF003103

Dietterich HR, Soule SA, Cashman KV, Mackey BH (2015) Lava flows in 3D: using airborne lidar and preeruptive topography to evaluate lava flow surface morphology and thickness in Hawai'i. In: Hawaiian Volcanoes: from source to surface, geophysical monograph 208. Wiley, pp 483–505

Dietterich HR, Lev E, Chen J, Richardson JA, Cashman KV (2017) Benchmarking computational fluid dynamics models of lava flow simulation for hazard assessment, forecasting, and risk management. J Appl Volcanol 6:9. https://doi.org/10.1186/s13617-017-0061-x

Dietterich HR, Patrick M, Diefenbach A, Parcheta C, Lev E, Foks N (2018) Lava flow hazard modeling and the assessment of effusion rates and topographic change with UAS and lidar during the 2018

Kilauea lower East Rift Zone eruption, American Geophysical Union Fall Meeting Abstracts V21B-03

Favalli M, Pareschi MT, Neri A, Isola I (2005) Forecasting lava flow paths by a stochastic approach. Geophys Res Lett 32:L03305. https://doi.org/10.1029/2004GL021718

Favalli M, Chirico GD, Papale P, Pareschi MT, Boschi E (2009) Lava flow hazard at Nyiragongo volcano, D.R.C. Bull Volcanol 71(4): 363–374

Favalli M, Targuini S, Fornaciai A, Boschi E (2012) Dispersion index of topographic surfaces. Geomorphology 153-153:169–178

Ferrier KL, Huppert KL, Perron JT (2013a) Climatic control of bedrock river incision. Nature 496:206–209. https://doi.org/10.1038/nature11982

Ferrier KL, Perron JT, Mukhopadhyay S, Rosener JD, Stock JD, Hupper KL (2013b) Covariation of climate and long-term erosion rates across a steep rainfall gradient on the Hawaiian island of Kaua'i. Geol Soc Am Bull 125:1146–1163. https://doi.org/10.1130/B30726.1

Freeman TH (1991) Calculating catchment area with a divergent flow based on a regular grid. Comput Geosci 17:413–422. https://doi.org/10.1016/0098-3004(91)90048-I

Griffiths RW (2000) The dynamics of lava flows. Annu Rev Fluid Mech 32:477–518. https://doi.org/10.1146/annurev.fluid.32.1.477

Guest JE, Kilburn CRJ, Pinkerton H, Duncan AM (1987) The evolution of lava flow-fields: observations of the 1981 and 1983 eruptions of Mount Etna, Sicily. Bull Volcanol 49:527–540. https://doi.org/10.1007/BF01080447

Harris AJL (2013) Lava flows. In: Lava flows. Modeling volcanic processes: the physics and mathematics of volcanism. Cambridge University Press, New York, pp 85–106

Harris AJ, Rowland S (2001) FLOWGO: a kinematic thermo-rheological model for lava flowing in a channel. Bull Volcanol 63:20–44. https://doi.org/10.1007/s004450000120

Harris, AJL, Rowland SK (2009) Effusion rate controls on lava flow length and the role of heat loss: a review. Studies in volcanology: the legacy of George Walker. Special publications of IAVCEI, 2 :33–51

Harris AJL, Favalli M, Wright R, Garbeil H (2011) Hazard assessment at Mount Etna using a hybrid lava flow inundation model and satellite-based land classification. Nat Hazards 58:1001–1027. https://doi.org/10.1007/s11069-010-9709-0

Hon K, Kauahikaua J, Denlinger R, Mackay K (1994) Emplacement and inflation of pahoehoe sheet flows: observations and measurements of active lava flows on Kilauea Volcanon, Hawaii. Bull Geol Soc Am 106(3):351–370

Huang J, Turcotte DL (1990) Fractal image analysis: application to the topography of Oregon and synthetic images. J Opt Soc Am A 7: 1124. https://doi.org/10.1364/JOSAA.7.001124

Hulme G, (1974) The Interpretation of Lava Flow Morphology. Geophysical Journal International 39(2):361-383

Ishihara K, Iguchi M, Kamo K (1990) Numerical simulation of lava flows on some volcanoes in Japan. In: Lava flows and domes. Springer, Berlin, Heidelberg, pp 174–207

Karlstrom L, Richardson PW, O'Hara D, Ebmeier SK (2018) Magmatic landscape construction. J Geophys Res Earth Surf 123. https://doi.org/10.1029/2017JF004369

Katz MG, Cashman KV (2003) Hawaiian lava flows in the third dimension: identification and interpretation of pahoehoe and 'a'a distribution in the KP-1 and SOH-4 cores. Geochem Geophys Geosyst 4. https://doi.org/10.1029/2001GC000209

Kauahikaua J, and the Hawaiian Volcano Observatory staff (2016) The 2014 annual report for the Hawaiian Volcano Observatory. U.S. Geological Survey Scientific Investigations Report 2016-5059, 65 p. https://doi.org/10.3133/sir20165059

Kerr RC, Griffiths RW, Cashman KV (2006) Formation of channelized lava flows on an unconfined slope. J Geophys Res 111:B10206. https://doi.org/10.1029/2005JB004225

Kilburn CRJ (1981) Pahoehoe and aa lavas: a discussion and continuation of the model of Peterson and Tilling. J Volcanol Geotherm Res 11: 373–382. https://doi.org/10.1016/0377-0273(81)90033-0

Kolzenburg S, Giordano D, Cimarelli C, Dingwell DB (2016) In situ thermal characterization of cooling/crystallizing lavas during rheology measurements and implications for lava flow emplacement. Geochim Cosmochim Acta 195:244–258. https://doi.org/10.1016/J.GCA.2016.09.022

Kubanek J, Richardson JA, Charbonnier SJ, Connor LJ (2015) Lava flow mapping and volume calculations for the 2012–2013 Tolbachik, Kamchatka, fissure eruption using bistatic TanDEM-X InSAR. Bull Volcanol 77:106. https://doi.org/10.1007/s00445-015-0989-9

Levandowsky M, Winter D (1971) Distance between Sets. Nature 234: 34–35. https://doi.org/10.1038/234034a0

Lipman PW, Banks NG (1987) A'a flow dynamics, Mauna Loa, 1984. US Geol Surv Prof Pap 1350:1527–1567

Lohse KA, Dietrich WE (2005) Contrasting effects of soil development on hydrological properties and flow paths. Water Resour Res 41. https://doi.org/10.1029/2004WR003403

Mossoux S, Saey M, Bartolini S, Poppe S, Canters F, Kervyn M (2016) Q-LAVHA: a flexible GIS plugin to simulate lava flows. Comput Geosci 97:98–109

Murphy BP, Johnson JPL, Gasparini NM, Sklar LS (2016) Chemical weathering as a mechanism for the climatic control of bedrock river incision. Nature 532:223–227. https://doi.org/10.1038/nature17449

O'Hara D, Karlstrom L, Roering JJ (2019) Distributed landscape response to localized uplift and the fragility of steady states. Earth Planet Sci Lett 506:243–254

Patrick MR, Kauahikaua J, Orr T, Davies A, Ramsey M (2016) Operational thermal remote sensing and lava flow monitoring at the Hawaiian Volcano Observatory. Geol Soc Lond Spec Publ 426:489–503. https://doi.org/10.1144/SP426.17

Perron JT, Kirchner JW, Dietrich WE (2008) Spectral signatures of characteristic spatial scales and nonfractal structure in landscapes. J Geophys Res 113:F04003. https://doi.org/10.1029/2007JF000866

Peterson DW, Tilling RI (1980) Transition of basaltic lava from pahoehoe to aa, Kilauea Volcano, Hawaii: field observations and key factors. J Volcanol Geotherm Res 7(3–4):271–293

Pieri DC, Baloga SM (1986) Eruption rate, area, and length relationships for some Hawaiian lava flows. J Volcanol Geotherm Res 30:29–45. https://doi.org/10.1016/0377-0273(86)90066-1

Pinkerton H, Wilson L (1994) Factors controlling the lengths of channel-fed lava flows. Bull Volcanol 56:108–120. https://doi.org/10.1007/BF00304106

Poland MP (2014) Time-averaged discharge rate of subaerial lava at Kīlauea Volcano, Hawai'i, measured from TanDEM-X interferometry: implications for magma supply and storage during 2011-2013. J Geophys Res Solid Earth 119:5464–5481. https://doi.org/10.1002/2014JB011132

Poland MP, Orr TR, Kauahikaua JP, Brantley SR, Babb JL, Patrick MR, Neal C, Anderson KR, Antolik L, Burgess MK, Elias T, Fuke S, Fukunaga P, Johanson I, Kagimoto M, Kamibayashi KP, Lee L, Miklius A, Million W, Moniz CJ, Okubo PG, Sutton A, Takahashi TJ, Thelen WA, Tollett W, Trusdell FA (2016) The 2014–2015 Pāhoa lava flow crisis at Kīlauea Volcano, Hawai'i: disaster avoided and lessons learned. GSA Today:4–10. https://doi.org/10.1130/GSATG262A.1

Press WH, Teukolsky SA, Vetterling WT, Flannery BP (2007) Numerical recipes: the art of scientific computing, 3rd edn. Cambridge University Press ISBN-13:9780521880688

Quinn P, Beven K, Chevallier P, Planchon O (1991) The prediction of hillslope flow paths for distributed hydrological modelling using

digital terrain models. Hydrol Process 5(1):59–79. https://doi.org/10.1002/hyp.3360050106

Richter N, Favalli M, de Zeeuw-Van Dalfsen E, Fornaciai A, da Silva Fernandes RM, Pérez NM, Levy J, Victória SS, Walter TR (2016) Lava flow hazard at Fogo Volcano, Cabo Verde, before and after the 2014–2015 eruption. Hazards Earth Syst Sci 16:1925–1951. https://doi.org/10.5194/nhess-16-1925-2016

Riker JM, Cashman KV, Kauahikaua JP, Montierth CM (2009) The length of channelized lava flows: insight from the 1859 eruption of Mauna Loa Volcano, Hawai'i. J Volcanol Geotherm Res 183:139–156. https://doi.org/10.1016/J.JVOLGEORES.2009.03.002

Robertson JC, Kerr RC (2012) Solidification dynamics in channeled viscoplastic lava flows. J Geophys Res 117:B07206

Roering JJ, Mackey BH, Marshall JA, Sweeney KE, Deligne NI, Booth AM, Handwerger AL, Cerovski-Darriau C (2013) 'You are HERE': connecting the dots with airborne lidar for geomorphic fieldwork. Geomorphology 200:172–183. https://doi.org/10.1016/j.geomorph.2013.04.009

Rumpf ME, Lev E, Wysocki R (2018) The influence of topographic roughness on lava flow emplacement. Bull Volcanol 80:63

Schwanghart W, Kuhn NJ (2010) TopoToolbox: a set of Matlab functions for topographic analysis. Environ Model Softw 25:770–781. https://doi.org/10.1016/J.ENVSOFT.2009.12.002

Sherrod DR, Sinton, JM, Watkins, SE Brunt, KM (2007) Geologic map of the state of Hawai 'i: US Geological Survey Open-File Report 2007–1089. Available online at URL: http://pubs.usgs.gov/of/2007/1089

Simons FJ (2009) Slepian functions and their use in signal estimation and spectral analysis. In: Freeden W, Nashad MZ, Sonar T (eds) Handbook of geomathematics. Springer, Berlin, pp 891–923

Slezin YB (2008) Two types of lava fields and the mechanism of their generation. J Volcanol Seismol 2:340–346. https://doi.org/10.1134/S0742046308050035

Soldati A, Sehlke A, Chigna G, Whittington A (2016) Field and experimental constraints on the rheology of arc basaltic lavas: the January 2014 Eruption of Pacaya (Guatemala). Bull Volcanol 78:43. https://doi.org/10.1007/s00445-016-1031-6

Soule SA, Cashman KV, Kauahikaua JP (2004) Examining flow emplacement through the surface morphology of three rapidly emplaced, solidified lava flows, Kilauea Volcano, Hawai'i. Bull Volcanol 66:1–14. https://doi.org/10.1007/s00445-003-0291-0

Tarboton DG (1997) A new method for the determination of flow directions and upslope areas in grid digital elevation models. Water Resour Res 33:309–319. https://doi.org/10.1029/96WR03137

Tarquini S, Favalli M (2011) Mapping and DOWNFLOW simulation of recent lava flow fields at Mount Etna. J Volcanol Geotherm Res 204:27–39. https://doi.org/10.1016/J.JVOLGEORES.2011.05.001

Trusdell FA, Wolfe EW, Morris J (2005) Digital database of the geologic map of the island of Hawai'i. DS 144. US Geological Survey, Reston, VA

Vicari A, Alexis H, Del Negro C, Coltelli M, Marsella M, Proietti C (2007) Modeling of the 2001 lava flow at Etna volcano by a cellular automata approach. Environ Model Softw 22:1465–1471. https://doi.org/10.1016/J.ENVSOFT.2006.10.005

Wadge G, Young PAV, McKendrick IJ (1994) Mapping lava flow hazards using computer simulation. J Geophys Res Solid Earth 99(B1):489–504

Walker GPL (1971) Compound and simple lava flows and flood basalts. Bull Volcanol 35(3):579–590

Walker GPL (1973) Mount Etna and the 1971 eruption - lengths of lava flows. Philos Trans R Soc Lond A 274:107–118. https://doi.org/10.1098/rsta.1973.0030

Wegmann KW, Zurek BD, Regalla CA, Bilardello D, Wollenberg JL, Kopczynski SE, Ziemann JM, Haight SL, Apgar JD, Zhao C, Pazzaglia FJ (2007) Position of the Snake River watershed divide as an indicator of geodynamic processes in the greater Yellowstone region, western North America. Geosphere 3:272. https://doi.org/10.1130/GES00083.1

Whiting PJ, Moog DB (2001) The geometric, sedimentologic and hydrologic attributes of spring-dominated channels in volcanic areas. Geomorphology 39:131–149. https://doi.org/10.1016/S0169-555X(00)00103-3

Wolfe EW, Neal CA, Banks NG, and Duggan TJ, (1988) Geologic observations and chronology of eruptive events, ch. 1 of Wolfe EW, ed., The Puu Oo eruption of Kilauea Volcano, Hawaii; episodes 1 through 20, Jan 3, 1983, through June 8: U.S. Geological Survey Professional Paper 1463, p. 1–97.

Young P, Wadge G (1990) FLOWFRONT: simulation of a lava flow. Comput Geosci 16:1171–1191